Chemical Engineering Journal 446 (2022) 137352

Contents lists available at ScienceDirect

Chemical Engineering Journal

journal homepage: www.elsevier.com/locate/cej

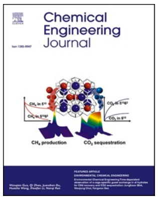

Enhanced peroxymonosulfate activation in the morphotropic phase boundary of molybdenum doped $LaCoO_{3-\delta}$ perovskite

Yu Shen [a], María J. Martín de Vidales [a], Giulio Gorni [b], María J. Rivero [c], Inmaculada Ortiz [c], Antonio J. Dos santos-García [a,*]

[a] *Departamento de Ingeniería Mecánica, Química y Diseño industrial. Escuela Técnica Superior de Ingeniería y Diseño Industrial, Universidad Politécnica de Madrid, 28012 Madrid, Spain*
[b] *CELLS-ALBA Synchrotron Light Facility, 08290 Cerdanyola del Vallès, Spain*
[c] *Departamento de Ingenierías Química y Biomolecular, Universidad de Cantabria, 39005 Santander, Spain*

ARTICLE INFO

Keywords:
Advanced oxidation process
Peroxymonosulfate
Perovskite
Oxidation state
Morphotropic phase boundary

ABSTRACT

Perovskite oxides, with an ABO_3 general formula, have attracted much attention as effective peroxymonosulfate (PMS) activators because of their composition adjustability and chemical stability. A doping strategy has been applied to enhance the PMS activation capability with the modulation of the crystal structure of the parent $LaCoO_{3-\delta}$ perovskite by substituting Co atoms located at the B-site, with high valence state transition metals. Herein, a series of $LaCo_{1-x}Mo_xO_{3-\delta}$ perovskites were prepared with different Mo content, showing a phase transformation from rhombohedral to cubic-like structures. $LaCo_{0.95}Mo_{0.05}O_{3-\delta}$ compound is located at the so-called morphotropic phase boundary (MPB) boosting PMS activation performance as well as enhanced stability. The presence of local inhomogeneities, observed as oxygen vacancies, has been detected in the MPB region enhancing the catalytic effect of pollutant degradation. Mo doping induced Co reduction that contributed to the enhanced PMS activation. Sulfate radical was identified to be the dominating reactive specie for $LaCo_{1-x}Mo_xO_{3-\delta}$ catalyzed PMS activation. This work contributes first, to clarifying the role of Mo doping to boost PMS activation, and second to highlighting the crucial role of the reduced oxidation state as well as the oxygen vacancies in the MPB for PMS activation. Impressive results were obtained when $LaCo_{0.95}Mo_{0.05}O_{3-\delta}$ compound was deposited in a Lab-grade photoreactor with LED technology, reaching a complete removal of paracetamol in the first minute. This study provided new insight into the rational design of PMS activator and developed a new strategy for heterogeneous active PMS at a photoreactor with immobilized catalysts.

1. Introduction

In recent years, various pharmaceuticals have been detected in effluents and natural waters throughout the world, which have aroused wide concern about their potential effects on the environment and human health [1]. As one kind of the most effective analgesics and antipyretic drugs, paracetamol has been heavily used and was found to exist in wastewater treatment effluents and surface waters in μg/L [2]. Therefore, it is highly demanded to develop effective remediation techniques to avoid the accumulation of pharmaceuticals in the water environment. Advanced oxidation processes (AOPs) have been investigated as promising alternatives for the degradation of organic contaminants in the water environment [3–6]. During the past decade, peroxymonosulfate (PMS) based advanced oxidation processes attracted extensive attention because of the generation of reactive oxygen species (ROS) from the cleavage of the peroxide bond in HSO_5^- via heat, ultraviolet irradiation, transition metals catalysis [7–9] and its high efficiency within a wide pH range [10–12]. Among various activation techniques, transition metal-based heterogeneous catalysts have shown great potential because of their widely operating conditions, needless of extra energy and high efficiency, mainly due to the in situ generation of oxidant radicals ($SO_4\bullet^-$, •OH, etc.) as well as nonradical oxidation pathways (electron transfer, Fe/Co-oxo complexes, etc.) [13–15]. In the heterogeneous catalytic PMS activation, Co-based catalysts have been determined to be highly efficient and the catalytic capability can be further promoted [16]. However, due to the inherent toxicity of Co, the proper heterogeneous catalysts should be stabilized in stable crystal structures to minimize Co leaching and avoid secondary pollution.

---

* Corresponding author.
E-mail address: aj.dossantos@upm.es (A.J. Dos santos-García).

https://doi.org/10.1016/j.cej.2022.137352
Received 1 April 2022; Received in revised form 19 May 2022; Accepted 1 June 2022
Available online 2 June 2022

Recently, perovskite oxides, with the chemical formula of ABO_3, have emerged as promising candidates for heterogeneous PMS activation [17,18]. The A-site cations are normally larger in size than the B-site cations, which are surrounded by six oxygen anions in octahedral coordination [19]. Ideal ABO_3 perovskite crystallizes in the cubic *Pm*-3 *m* structure but substitutional derivatives occurring at A-, B- or both sites $(AA')(BB')O_6$ reduce the crystal symmetry of the parent compound [20]. Therefore, a phase transformation as a function of composition may occur and the character of the phase transition also termed morphotropic phase boundary (MPB), can be related to the enhancement of the physical properties of the compounds. For instance, isotropic displacements of Zr and Ti in the perovskite $PbZrO_3$-$PbTiO_3$ solid solution are the responsible of the enhanced ferroelectric properties at the MPB [21] and the concentration of oxygen vacancies is the responsible of the conduction behavior in the $(Pb_{1-x}Ba_x)(Zr_{0.95}Ti_{0.05})O_3$ system [22]. Various cobalt-based perovskite oxides ($LaCoO_3$ [23–25], $La_{0.8}Sr_{0.2}CoO_{3-\delta}$ [26], $SrCo_{1-x}Ti_xO_3$ [27], $Gd_xLa_{1-x}BaCo_2O_6$ [28], $La_{0.5}Ba_{0.5}Co_xMn_{1-x}O_{3-\delta}$ [29], $PrBaCo_2O_{5+\delta}$ [30], etc.) have been reported to be efficient PMS activators. The PMS activation capabilities were found to be mainly related to the electronic states of Co ions, where Co^{2+} was usually considered to pose higher activity [24,31]. Even though A-site substitution may lead to the change of oxidation states in B-site, the relative low oxidation states of common A-site ions (+1, +2 or + 3) make it difficult to obtain perovskite with reduced Co oxidation state via A-site doping. Considering the more flexible variation of valence state in B-sites transition metals (TMs), substituting Co for TMs is more feasible to manipulate the electronic structure of Co. In this case, Mo^{6+} could to be an ideal candidate for Co substitution due to its high stable oxidation state with similar ionic radius in octahedral coordination (0.59 Å of Mo^{6+} *vs.* 0.545 Å of Co^{3+}) [32]. Moreover, PMS activation could be further enhanced by the formation of Co-O-M bonds to accelerate the electron transfer between the redox couples [33]. Despite this, exploring suitable dopants to rationally design catalysts is still challenging and the mechanism of enhanced PMS activation performance remains uncertain.

Herein, Mo is introduced into the B-site of $LaCoO_{3-\delta}$ to reduce the Co valence state mainly affordable by the similar ionic radii of Mo^{6+} and Co^{2+}/Co^{3+}. Concomitantly to the cationic doping a phase transformation from *R*-3*c* to *Pm*-3 *m* occurs giving rise to a continuous MPB at a 5% Mo-doping composition. The $LaCo_{1-x}Mo_xO_{3-\delta}$ obtained compounds led to promoted activation of PMS and enhanced stability benefited from the reduction of Co oxidation state. A degradation pathway, dominated by the $SO_4\bullet^-$ radicals, has been further identified and the enhanced properties of the $LaCo_{0.95}Mo_{0.05}O_{3-\delta}$ phase are associated with the presence of local oxygen vacancies at the MPB. This work reveals the importance of oxidation state and oxygen vacancies, which may be constructive for the rational design of a PMS activator in the vicinity of a MPB. Furthermore, experiments have been conducted with a suspended and deposited catalyst to compare the process efficiency and the advantages and disadvantages of the different systems. The influence of UV light LEDs radiation (UVA and UVC) and PMS concentration are also studied in a Lab-grade photoreactor with LED technology, confirming the applicability of the prepared catalyst.

2. Materials and methods

2.1. Chemicals

$La(NO_3)_3\cdot 6H_2O$ (99.9%), $Co(NO_3)_2\cdot 6H_2O$ (99 %), $(NH_4)_6Mo_7O_{24}\cdot 4H_2O$ and citric acid (99%) were used for the catalysts preparation. Paracetamol (99%), potassium peroxymonosulfate ($KHSO_5\cdot 0.5KHSO_4\cdot 0.5K_2SO_4$, PMS), 5,5-Dimethyl-1-pyrroline N-oxide (DMPO), 2,2,6,6-tetramethylpiperidine (TEMP), radical scavengers (methanol (MeOH, >99.9 %), tertiary butyl alcohol (TBA, 99 %) and furfuryl alcohol (FFA, 98 %)), Nafion 5 wt% and ethanol (>99.5%) (used for ink electrode preparation) were obtained from Sigma-Aldrich. Additional auxiliary reagents H_2SO_4 (98 %), NaOH (98 %), Na_2CO_3 (99.5 %), NaCl (99 %), $NaNO_3$ (99 %), and $NaHCO_3$ (99 %) were supplied by Panreac Química S.A. (Barcelona, Spain). All reagents were used without further purification. Deionized and ultrapure water was used throughout all degradation experiments.

2.2. Synthesis of catalysts

$LaCo_{1-x}Mo_xO_{3-\delta}$ (x = 0, 0.05, 0.1 and 0.2, denoted as LCO, LCMO005, LCMO010 and LCMO020, respectively) were synthesized via sol–gel method. Stoichiometric amounts of $La(NO_3)_3\cdot 6H_2O$, $Co(NO_3)_2\cdot 6H_2O$ and $(NH_4)_6Mo_7O_{24}\cdot 4H_2O$ (10 mmol in total) were weighted and dissolved in 20 mL of deionized water with 20 mmol of citric acid as complexing agent. The resultant mixture was heated at 80 °C under continuous magnetic stirring until the gel was formed. The obtained gel was further dried in an oven at 110 °C for 12 h. Afterward, the precursor was transferred to a crucible and annealed in a furnace at 700 °C for 5 h with a heating rate of 5 °C/min in air. The obtained products were thoroughly ground into fine powder for degradation experiments. For the deposition of the catalyst on a cylindrical Ti surface, two mixtures of 126.6 mg of catalyst, 271.25 mg of Nafion 20 wt% and 40.5 g of isopropanol (>99.5%), used as a solvent, were prepared and sonicated for 45 min. The mixtures were sprayed on the Ti surface with an airbrush under heating, in order to evaporate the solvent, with control of the sprayed area (0.032 m^2).

2.3. Characterization

The crystal structure of the prepared catalysts was determined by X-ray powder diffraction (XRD) using a Phillips XPert PRO ALPHA 1 diffractometer using Cu $K\alpha_1$ radiation operating with a step-width of 0.017°. The corresponding Rietveld refinements were performed with FullProf program [34]. High-resolution transmission electron microscopy (HRTEM) and selected-area electron diffraction (SAED) was performed on a JEOL JEM 2100 operating at 200 kV equipped with an X-ray energy-dispersive spectrometer (EDS) OXFORD INCA for the compositional analysis of each investigated crystal by in situ observations. The Brunauer-Emmett-Teller (BET) surface area was calculated by measuring the N_2 adsorption–desorption isotherms at 77 K in a Micromeritics ASAP 2020 adsorption analyzer. X-ray absorption spectroscopy (XAS) measurements were performed at the CLÆSS beamline of the ALBA synchrotron. The optimal mass of sample powder was mixed with cellulose and pressed to pellets for measurements in transmission mode at room temperature. Co and Mo foils were used for energy calibration while CoO, Co_3O_4, MoO_2, and MoO_3 were also measured in transmission mode and used as reference compounds for Co and Mo K-edge, respectively. The analysis of XANES (X-ray absorption near-edge structure) and EXAFS (extended X-ray absorption fine structure) data was performed using ATHENA and ARTEMIS software of the DEMETER package [35]. The surface chemical states were investigated by X-ray photoelectron spectroscopy (XPS) using a PHI VersaProbe II instrument with a monochromatic Al Kα source. The oxygen deficiencies in $LaCo_{1-x}Mo_xO_{3-\delta}$ (x = 0, 0.05, and 0.1) were estimated by iodometric titration and the procedure was provided in Text S1. The magnetic susceptibility was measured in the temperature range 5–300 K, using a superconducting quantum interference device (SQUID) XL-MPMS magnetometer (Quantum Design, San Diego, CA, USA) under zero-field-cooling (ZFC) and field-cooling (FC) conditions with the DC magnetic field of 1000 Oe. Magnetization measurements as a function of the applied magnetic field (H) were performed at 300 K at magnetic fields up to 5 T. All the electrochemical characterizations were performed on an Autolab PGSTAT302 N using a three electrodes cell with a Pt wire as a counter electrode and Ag/AgCl as a reference electrode. A circular glassy carbon (area 0.196 cm^2) was used as a working electrode by dropping 10 μL of conductive ink, prepared as follows. 10 mg conductive carbon and 10 mg catalysts were added into 0.1 mL Nafion solution (5 wt%) and 1 mL of absolute ethanol. The open-circuit potential (OCP) was monitored for a total time of 1200 s at galvanostatic mode. Chronoamperometries were conducted at the bias of 0.0 V *vs* Ag/AgCl during a total time of 1200 s. During OCP and Chronoamperometry measurements, 1 mL of 0.325 M PMS solution and 1 mL of 1 g/L paracetamol solution was added at 200 s and 700 s, respectively. Electrochemical impedance spectroscopy (EIS) was conducted with frequencies of 0.01–100 kHz and 10 mV of amplitude perturbation. 100 mL of Na_2SO_4 (0.1 M) solution with 3.25 mM of PMS was used as the electrolyte in EIS measurements while chronoamperometry and OCP measurements were conducted without PMS in the initial electrolyte.

2.4. Experimental procedure

Batch experiments with suspended catalyst were conducted in 250 mL beakers at 25 ± 0.5 °C with constant stirring of 300 rpm. In each experiment, specific amounts of PMS and catalyst were added to 100 mL of 10 mg/L of paracetamol solution. The initial pH was adjusted by dropping HNO_3 and NaOH of 0.1 M concentration. 1 mL of solution samples was regularly withdrawn at given time intervals and filtered through 0.45 μm cellulose filters. Afterward, the samples were mixed with 0.5 mL MeOH to quench the degradation reaction and analyzed by the high-performance liquid chromatography (HPLC) to determine the residual paracetamol concentrations. To test the reusability of the catalyst, the solution after the reaction was filtered using 0.45 μm cellulose filter followed by washing to collect the catalyst. The filter was then dried at 80 °C overnight to be used in the next cycle. A chemical probe method was firstly used by combining different radical scavenger reagents (TBA, MeOH, and FFA) to investigate the presence of different reactive oxygen species (ROS). The effect of the presence of additional ions during the degradation process was tested by introducing 2 mM NaCl, $NaNO_3$ and $NaHCO_3$ as HCO_3^-, NO_3^- and Cl^- anion sources. The presence of radicals was also confirmed by electron spin resonance (ESR) as described in the analytical section. Experiments with deposited catalysts were carried out with photocatalysis equipment provided with LED technology Photolab LED365-16, supplied by APRIA Systems, S.L. The wastewater was stored in a glass tank of 500 mL with agitation. The catalyst was deposited by spraying inside a hollow cylinder, to be exposed to the UV radiation source is placed (20 LEDs, UVA 365–370 nm, 1200 mW, 2100 W/m^2 or UVC 265–280 nm, 15 mW, 25 W/m^2). Temperature (°C), irradiance (W/m^2), intensity (mA), and the percentage of use of the LEDs (0–100%) were controlled. The samples were filtered with 0.45 μm Nylon filters before analysis.

2.5. Analysis method

For the experiments carried out with suspended catalyst, paracetamol concentration was measured using a HPLC Jasco MD-2010/2015 with a 5 μm C18 analytical column (4.6 mm × 250 mm) and UV/Vis detector. Paracetamol was quantified at a wavelength of 243 nm with a mobile phase of water/methanol (50/50 v/v %) at the flow rate of 1 mL/min. The column temperature was 25 ℃ and samples of 5 μL were injected. On the other hand, for the experiments conducted in the batch reactor with deposited catalyst, the concentration of paracetamol and of the generated intermediates were measured by HPLC-DAD (Agilent 1100 Series). The detector wavelength was 243 nm and the column temperature was 25 °C. The injection volume was set at 20 μL, and a Zorbax Extend-C18 5 μm analytical column (3.0 mm × 150 mm) was used. The mobile phase was acetonitrile/water (50/50 v/v %) with a flow rate of 0.6 mL/min. To further identify paracetamol degradation byproducts, the pure paracetamol solution (10 mg/L) and samples after catalytic degradation reaction (1, 5 and 10 min) were selected to be measured in a HPLC-MS chromatograph. Water (phase A) and methanol (phase B) were used as the mobile phase with a flow rate of 0.8 mL/min. Samples were separated via HPLC (Agilent 1100 Series) equipped with a 5 μm C18 analytical column (4.6 mm × 250 mm) at the elution gradient of 0–5 min, 0–20% B; 5–10 min, 20%-70% B; 10–15 min, 70% B; 15–20 min, 70%-0B; 20–25 min, 0B. The HPLC system was connected to a 6530 Q-TOF LC/MS (Agilent). MS data were obtained by a full scan mass from *m/z* 50–1000 under positive ion mode. The turbidity was measured with a HI 93,703 Microprocessor Turbidity Meter Hanna Instruments (range 0–1000 FTU). The concentration of PMS was spectrophotometrically determined using a modified iodometric titration method as described elsewhere [36]. All the measurements were duplicated and the average value was used. Error bars represent the standard deviation. The corresponding reaction rate constant was calculated using pseudo-first-order rate equation: $\ln(C/C_0) = - k_{obs} \bullet t$. Leached Co ions to the aqueous solutions were analyzed by Thermo Scientific iCE 3000 series atomic absorption spectroscopy (AAS) while leached Mo ions were analyzed by ICP-MS in a BRUKER Aurora Elite spectrometer. The involved radicals were recorded on a Bruker EMX X-band electron spin resonance (ESR) spectrometer (9.5 GHz) with 2,2,6,6-tethamethyl-4-piperidinol (TEMP) and 5,5-dimethyl-1-pyrrolidine N-oxide (DMPO) as spin trap agents. An indirect measurement of the surface perovskites-charge was carried out in dilute perovskite-supernatant after centrifugation of an aqueous dispersed sample by measuring the zeta potential (ζ), using a ZetaPlus instrument that exploits phase-analysis light scattering under electrophoretic particle migration of size range of 10 nm to 30 μm (Brookhaven Ltd.). It operates with a 35 mW solid state laser, red (660 nm wavelength) The ZetaPlus device is suitable for measurements at very low electrophoretic mobilities in dilute suspensions using special cuvettes with adding 1 mM of KNO3. Such measurements cover the range of typically ± 150 mV corresponding to mobilities as low as 10^{-8} m^2 / V·s. The electrophoretic mobilities were evaluated and then related to the zeta potential using the Smoluchowsky relationship [37].

3. Results and discussions

3.1. Characterization

The XRD patterns and the corresponding Rietveld refinement of the different catalysts are shown in Fig. 1a and Fig. S1. The obtained refined lattice parameters and agreement factors are summarized in Table S1. Both, a and b lattice parameters show a contraction contrary to the increase in the c-axis when the content of Mo increases. It has been reported that the dopant in perovskite could be existed in either A site or B site [38]. In this work, the radii of Mo^{6+} (0.59 Å) is similar with Co^{3+} (0.545 Å) and much smaller than La^{3+} (1.36 Å), thus the Mo would be preferencially located at the octahedral sites rather than cubo-octahedral voids [32]. The cell volume responded to the expected increase associated to the bigger size of Mo^{6+} (0.59 Å) than Co^{3+} (0.545 Å) in octahedral coordination. Furthermore, the substitution of Mo^{+6} produces a partial reduction from Co^{3+} to Co^{2+}, also higher in size (0.65 Å). Moreover, the characteristic diffraction peak at ~ 33° (see the magnification in Fig. 1a) gradually shifted to the lower angles with the increase of the Mo dopant content, suggesting that the substitution of Co by Mo increased the unit cell parameters. Undoped LCO compound crystallize in the *R*-3*c* rhombohedral space group and a structural phase transition from *R*-3*c* to the cubic *Pm*-3 *m* space group is observed for Mo doping levels higher than 5%. It is worth to note that very good agreements can be found in the fittings of LCMO005 to *R*-3*c* and cubic *Pm*-3 *m*, which is a clear indication of the presence of a MPB at this compositional range. This was further confirmed by variation of the Co-O distances which were obtained from Rietveld refinement (Fig. S2), wherein Co-O octahedral distances are shorter throughout the MPB increasing the crystal strain due to the compression of the octahedral. LCMO010 crystallizes in the cubic *Pm*-3 *m* space group and a further increase of the Mo content (LCMO020) leads to the formation of a nonstoichiometric $La_{1-x}Co_{1-y}Mo_yO_{3-\delta}$ cubic perovskite and La_2MoO_6 as secondary phase, indicating that the solubility limit was reached at room pressure. The calculated weight percentages obtained from the Rietveld fitting were 91.5 % and 8.5 %, respectively. The N_2 adsorption–desorption isotherms of different samples are shown in Fig. 1b. All isotherm patterns can be

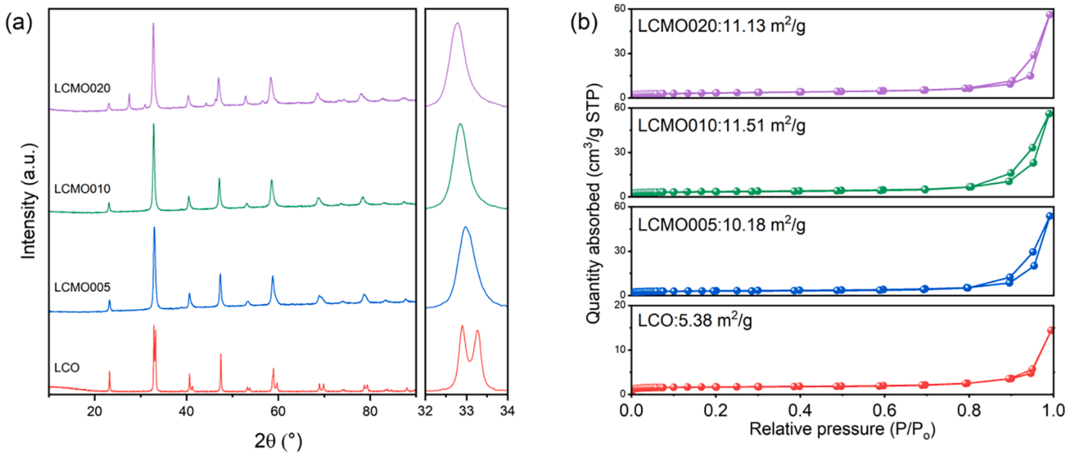

Fig. 1. XRD patterns (a) and N_2 adsorption–desorption isotherms (b) of LCO, LCMO005, LCMO010 and LCMO020.

assigned to type-IV shape with H3 hysteresis loops. LCO shows the lowest BET surface area value of 5.38 m^2/g and, after doping with 5 %, 10 % and 20 % Mo, the surface area significantly increased to 10.18, 11.15 and 11.13 m^2/g, respectively. Fig. 2a, 2b and 2c depict representative low magnification TEM images of LCO, LCMO005 and LCMO010, respectively, showing aggregates of perovskite nanoparticles around 50 nm diameter. The phase structures of LCO, LCMO005 and LCMO010 were further confirmed by HRTEM and corresponding FFT or SAED along [2–21] and [0 0 1] axes. The already observed superstructure spots in the FFT diagrams are due to double diffraction phenomena since there is no additional periodicity supporting cationic ordering. The semi-quantitative cationic contents, see Table S2, were checked by in situ EDS analyses (Fig. S3), demonstrating that the proportion between La, Co and Mo was in agreement with what was intended.

3.2. Catalytic performance of catalysts for PMS activation

Our previous studies have demonstrated that paracetamol cannot be efficiently degraded by using solo PMS [9] and only 2.5%, 3.9%, 4.6%, and 4.1% of paracetamol can be removed after 30 min by the action of LCO, LCMO005, LCMO010 and LCMO020 catalyzers without PMS, respectively (data not shown). These results suggest that the adsorption removal of paracetamol is negligible and correlates with the observed surface area of the solids. The performance of the catalytic PMS activation of LCO, LCMO005, LCMO010 and LCMO020 was evaluated in the experiments of paracetamol degradation with the catalyst suspended in the solution. As shown in Fig. 3a, the paracetamol removal efficiency was markedly promoted by the combined action of PMS and perovskite catalyzers indicating that, LCO and its derivative cubic perovskites are

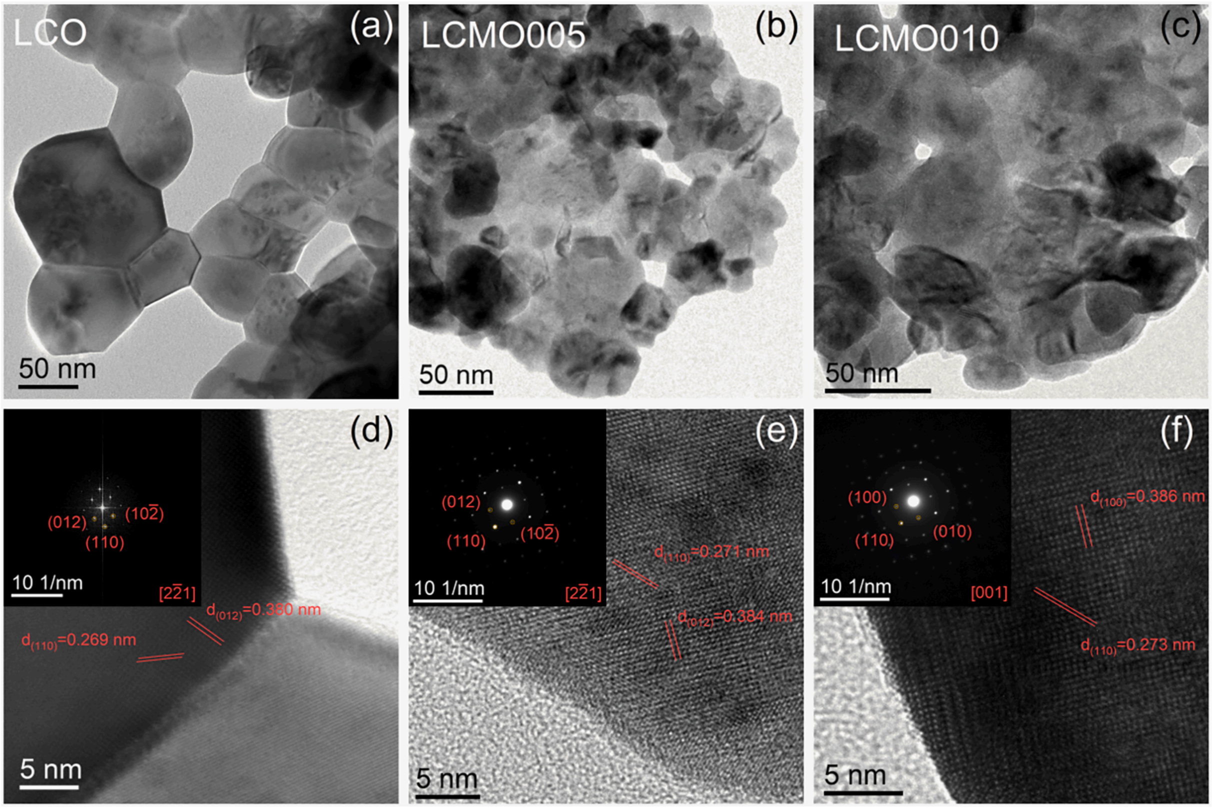

Fig. 2. TEM micrographs of LCO (a), LCMO005 (b) and LCMO010 (c); HRTEM micrographs of LCO (d) LCMO005 (e) and LCMO010 (f) (The inset shows corresponding FFT (for LCO) or SAED patterns (for LCMO005 and LCMO010)).

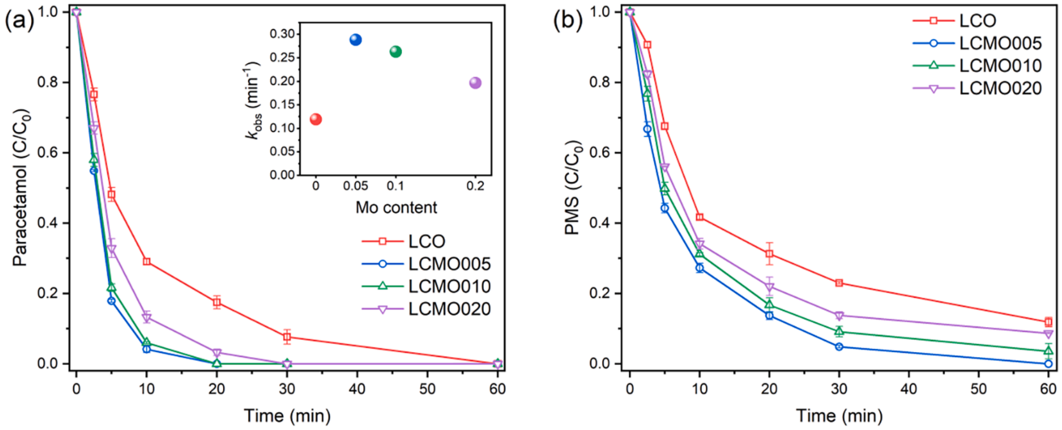

Fig. 3. Paracetamol removal (a) and PMS decomposition (b) with LCO, LCMO005, LCMO010 and LCMO020 (The inset shows corresponding reaction rate constant). Reaction conditions: [catalyst] = 0.2 g/L, [PMS] = 0.5 mM, [paracetamol] = 10 mg/L, temperature = 25 ± 0.5 °C, initial pH = 7 ± 0.2.

effective for the activation of PMS and, concomitantly to this, for pollutant degradation. Interestingly, the paracetamol removal is correlated to both, the crystal structure of the perovskites and to the specific surface area. LCO perovskite, showing the lowest symmetry and specific surface area, presents also the lowest kinetic constant for the degradation of the target pollutant. By introducing 5% Mo in B-cation sites of $LaCoO_{3-\delta}$, an increase in the crystal symmetry is induced and the reaction rate constant increases from 0.119 min^{-1} to 0.289 min^{-1}. However, keeping constant the crystal symmetry when increasing Mo dopant to 10% cannot further enhance the paracetamol removal efficiency, showing a similar rate constant of 0.263 min^{-1}. This can be understood taking into account that activation properties are enhanced across the MPB region. Compared to the other cubic perovskite phases, LCMO020 exhibits a weak PMS activation performance that can be attributed to the presence of the inert La_2MoO_6 phase reducing thereby the ratio of the active perovskite phase. It has to be taken into account that, the appearance of the La-rich secondary phase may lead to an A-cation site deficiency in the LCMO20 perovskite phase, that according to previous reports does not favor PMS activation [25]. Fig. 3b shows the results obtained from the spectrophotometric determination of PMS concentration at different activation times. The PMS decomposition rate followed the sequence LCMO005 > LCMO010 > LCMO020 > LCO, which

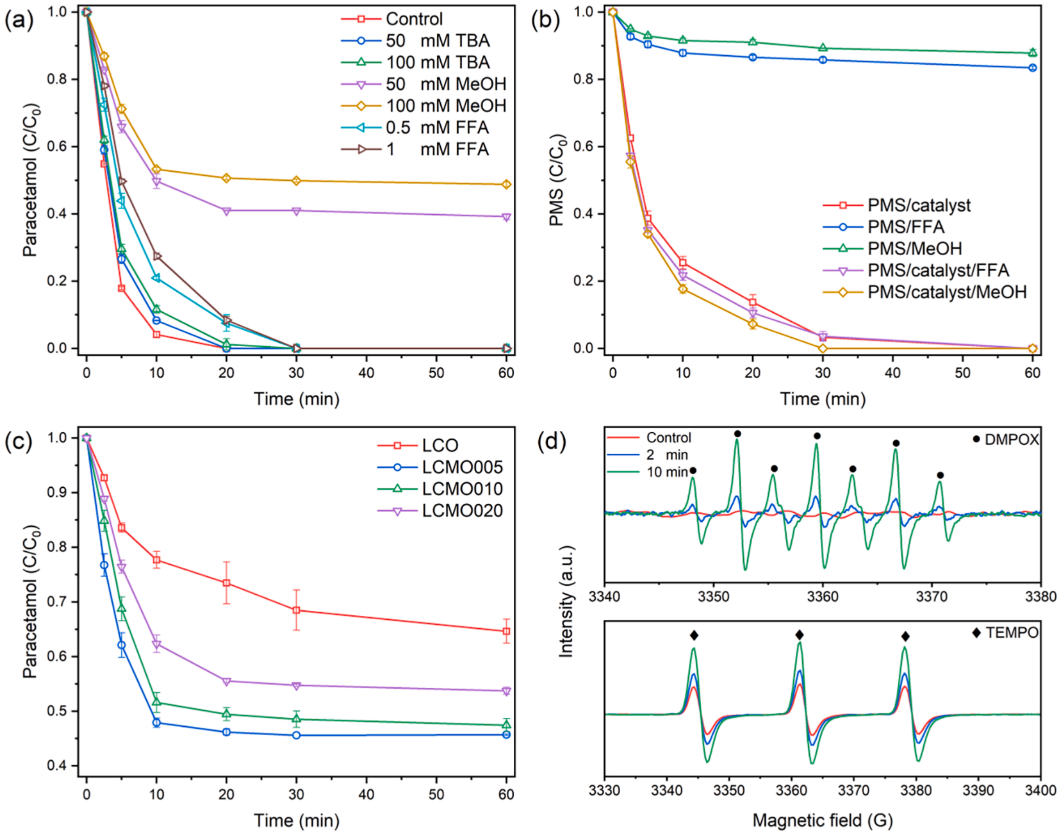

Fig. 4. (a) Effect of different radical scavengers on paracetamol removal with LCMO005 as catalyst. (b) Effect of FFA (1 mM) and MeOH (100 mM) on PMS decomposition with and without LCMO005 as catalyst. (c) Effect of MeOH (100 mM) on paracetamol removal with different catalysts (Notice that the y-axis scale starts at 0.4). (d) ESR spectra with 20 mM DMPO (top) and 20 mM TEMP (bottom) as spin trap agent and LCMO005 as catalyst. Reaction conditions: [catalyst] = 0.2 g/L, [PMS] = 0.5 mM, [paracetamol] = 10 mg/L, temperature = 25 ± 0.5 °C, initial pH = 7 ± 0.2.

was correlated to the paracetamol removal efficiency. It is worth noting that paracetamol degradation is faster than that found in PMS, suggesting an excess of oxidant concentration during the degradation experiments. Moreover, a 56.8% TOC removal was achieved after 60 min reaction with LCMO as a catalyst, indicating a notable mineralization degree of paracetamol, which was further confirmed by the LC-MS. Fig. S4 in the supplementary material shows the base peak chromatogram (BPC) of paracetamol catalytic oxidation products at different reaction times (1, 5 and 10 min). The peak assigned to the paracetamol dramatically declined over time while the emerging and vanishing of various degradation intermediates can be observed. The reported Co-based perovskite PMS activator and other Co-based PMS activators towards paracetamol degradation were also listed for comparison (Table S3), showing the excellent performance of Mo doped LCO.

3.3. ROS identification and proposed PMS activation mechanism

To identify the major ROS involved in paracetamol removal, the quenching experiments were conducted with MeOH, TBA and FFA as scavengers for •OH, SO_4•$^-$ and singlet oxygen ($^1O_2$). It is well known that TBA possesses high reactivity with •OH and, as depicted in Fig. 4a, slightly inhibited paracetamol removal at 50 mM and 100 mM TBA concentrations, suggesting that free •OH does not contribute substantially to the degradation process. Previous studies suggested that $^1O_2$ may also participate in the degradation process since some perovskites are also able to catalyze PMS activation [39,40]. Therefore, FFA was employed as $^1O_2$ scavenger to test this possibility. As shown in Fig. 4a, moderate concentration of FFA slightly inhibit paracetamol degradation, suggesting that $^1O_2$ participated, but didn't dominate paracetamol removal. However, paracetamol removal was significantly inhibited when 50 mM and 100 mM of MeOH were added, obtaining paracetamol removals of 60.2% and 51.7% in 60 min, respectively. We have also performed the study of the effect that chemical scavengers have in the PMS concentration in presence of the target pollutant. As shown in Fig. 4b, both MeOH and FFA cannot decompose PMS by themselves, thus discarding the existence of direct reaction with PMS to inhibit paracetamol removal. Our results are in good agreement with previous publications that have shown that TBA, FFA and MeOH have negligible effect on PMS decomposition [41]. Dramatic changes are observed in the PMS concentration by introducing the LCMO005 catalyst in the solution, what is indeed, a clear indication of the extremely high performance of the catalyst for PMS activation. Furthermore, by adding 100 mM of FFA or MeOH as radical scavengers, the PMS activation is kept, that is, PMS concentration decreases since SO_4•$^-$ are trapped by MeOH but they also oxidize paracetamol. Fig. 4c shows the PMS activation rate on different perovskite catalysts when MeOH is present as radical scavenger. As expected, the observed trend is correlated to that shown without scavengers, that is, the best pollutant degradation is reached by LCMO005 perovskite and the worst activation was accounted for the undoped LCO compound. Therefore, from the chemical probe experiments one can conclude that SO_4•$^-$ plays the most important role in the oxidation processes.

In order to confirm the chemical probe experiments, ESR measurements were further conducted to identify the generated radicals with DMPO and TEMP as spin trap agents. Fig. 4d (top part) shows that single PMS (control signal) cannot oxidize DMPO with a concentration of 0.5 mM. The characteristic signals of 5,5-dimethylpyrroline-(2)-oxyl-(1) (DMPOX) with an intensity ratio of 1: 2: 1: 2: 1: 2: 1 rather than DMPO-SO_4 (with the intensities of 1:1:1:1:1:1) were identified in presence of PMS and LCMO005, which can be attributed to the over-oxidation of DMPO by •OH or SO_4•$^-$ and/or the much more intensity of DMPOX compared with DMPO-SO_4 [42]. The TEMP has been widely employed as trap agent to detect the $^1O_2$. The typical TEMPO free radical signal (triplet signal with intensity of 1:1:1) appeared when solo PMS was added to the solution (control line), indicating that $^1O_2$ could come from PMS self-decomposition and not from other ROS (notice that no signal was detected in the DMPO EPR spectrum when using solo PMS). When LCMO005 was added to the solution, TEMPO signal increased its intensity along time, suggesting the continuous generation of $^1O_2$ from the catalyzed PMS decomposition. However, considering the limited increasing of TEMPO intensity with LCMO005, $^1O_2$ may not be the dominant ROS responsible of paracetamol degradation.

We have also explored the possibility of the existence of different degradation mechanisms. Direct electron transfer was previously reported to occur from organic pollutants (electron donor) to PMS (electron acceptor) with metal oxides as electron mediators [24,43]. To this end, we have investigated the electrochemical responses of the catalysts loaded working electrode to subsequent additions of PMS and paracetamol to the electrolyte solution. Fig. 5a shows the evolution of the open-circuit potential (OCP) for a total time of 1200 s at galvanostatic mode. It can be observed that the OCP significantly increased with PMS addition in all the tests, which was likely due to the adsorption of PMS on the working electrode leading to redistribution of the electron density and PMS activation [44]. The electrochemical activity of LCMO005 is, as expected, higher than that shown by other catalysts. However, the change in OCP was negligible when paracetamol was subsequently added. According to previous studies, the OCP changes with adding organic pollutants, thus implying the mediated electron transfer induced PMS decomposition [43,44]. Therefore, the electronic transfer process may not account for PMS activation and concomitantly to this, to paracetamol removal. Chronoamperometric measurements were further conducted at applied potential of 0 V *vs* Ag/AgCl to test the current responses to sequentially adding PMS and paracetamol. As shown in Fig. 5b, the current significantly decreased in all the tests with PMS addition showing LCMO005 the most pronounced signal. This could be interpreted as the fast electron transfer from catalyst to PMS, resulting in the PMS activation and radical generation. It was also noticed that the amount of current decreasing could be roughly correlated with paracetamol removal efficiency. The subsequently adding paracetamol did not lead to obvious current decreasing, which was consistent with previous OCP tests and excluded the PMS activation via mediated electron transfer. We have also tested EIS experiments to explore the charge transfer capacities of the different employed catalysts. As shown in Fig. S5, the smaller semicircle diameter in LCMO005 and LCMO010 Nyquist plots indicated weaker charge transfer resistance, which could indeed favor PMS activation.

The electronic structure of transition metals was generally considered to be correlated with the performance of PMS activation, thus XAS measurements were conducted following Co K-edge and Mo K-edge evolution to study changes in valence states and coordination environments. Fig. 6a shows the normalized X-ray absorption near edge structure (XANES) of perovskite samples and references measured at Co K-edge. The pre-edge feature around 7710 eV, associated to 1 s-3d transitions, remains unchanged for all the perovskite samples, suggesting a similar site symmetry around the absorbing atom [45]. The inset in Fig. 6a shows the magnification of the absorption edge, where the valence state of cobalt in different samples follows the trend LCO > LCMO005 > LCMO010 > LCMO020. This trend agrees well with our expectation that Co^{3+} in the undoped LCO compound, was further reduced with the increase of Mo content. It has been observed that, the degree of the reduction of Co^{3+} oxidation state was not proportional to Mo doping, that is, the reduction degree from LCO to LCMO005 is higher than that observed from LCMO005 to LCMO010. In order to check this anomalous behavior, we have carefully analyzed the XPS spectra for all the compounds since oxygen vacancies can be correlated to the so-called "oxygen lattice" and "surface oxygen" parameters. It is expected that a high "oxygen lattice"/ low "surface oxygen" components correlate to low oxygen vacancy content [46]. As shown in Fig. S6c, the O 1 s XPS spectra can be deconvoluted into up to 4 components, where the binding energy peaks at 528.6 eV, 529.8 eV, 531.3 eV and 532.8 eV can be attributed to lattice oxygen ions (O^{2-}, denoted as "lattice"), surface hydroxylation (denoted as "–OH"), adsorption oxygen species (O_2^-, O_2^{2-},

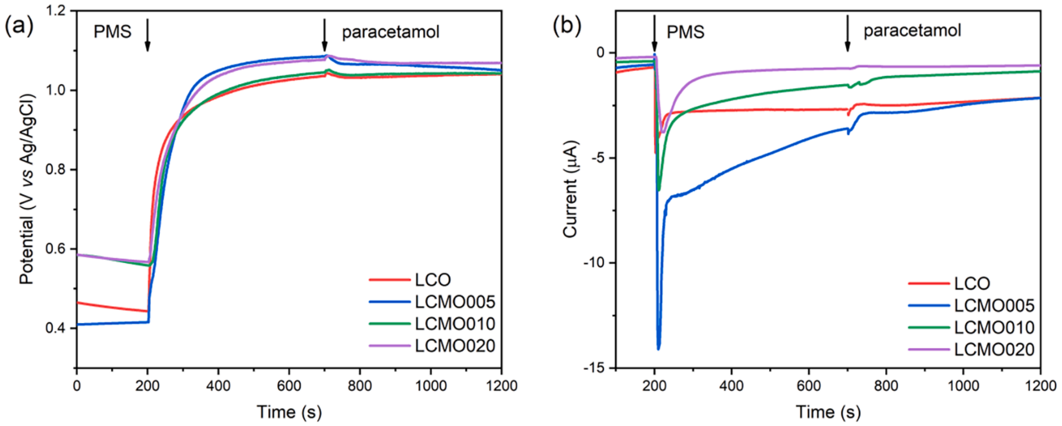

Fig. 5. Time dependent OCP curves (a) and chronoamperometry curves (b) of LCO, LCMO005, LCMO010 and LCMO020 ([PMS] = 3.25 mM, [paracetamol] = 10 mg/L, $[Na_2SO_4]$ = 100 mM, temperature = 25 ± 0.5 °C).

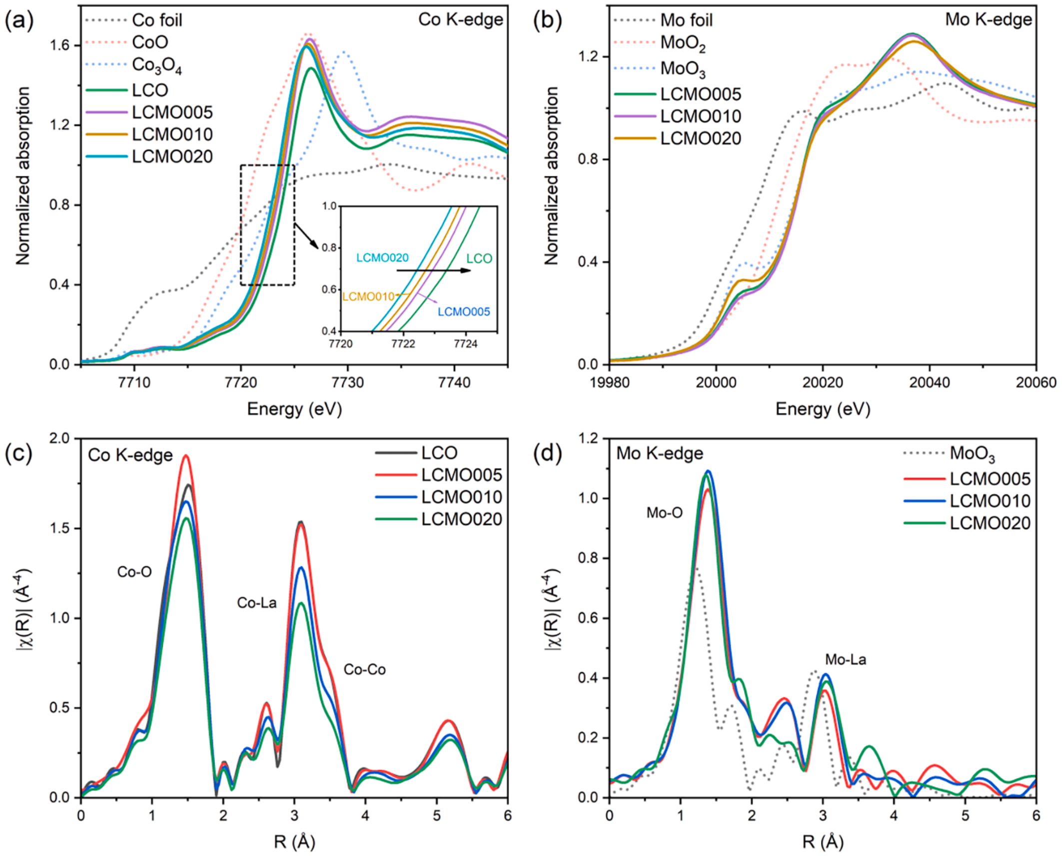

Fig. 6. Normalized XANES spectra at Co K-edge (a) and Mo K-edge (b) of reference compounds (dotted line) and samples (solid line) where the inset shows zoom of absorption edge of samples. Fourier transform moduli of $k^3\chi(k)$ spectra at Co K-edge (c) and Mo K-edge (d).

denoted as "surface") and adsorbed water (denoted as "$H_2O_{ads.}$"), respectively [47]. It can be observed that, the binding energy position and relative content illustrated in Table S4 indicates that the "surface" oxygen relative content and, therefore, oxygen vacancies, follows the order LCO > LCMO005 > LCMO010. One can conclude that, increasing Mo content from 5% to 10% may increase lattice oxygen even more than the 0% to 5% Mo doping step. To further determine the oxygen stoichiometry, we have also conducted iodometric titration and found the oxygen deficiencies to be 0.18,0.14 and 0.08 for LCO, LCO005 and LCMO010, respectively, which can be correlated to XPS and XANES analysis. This result is also confirmed by the features of pre-edge observed in the Mo K-edge.

The normalized XANES of different samples and references are shown in Fig. 6b at Mo K-edge. All the samples' spectra match the edge position of MoO_3 standard (20017 eV) suggesting that Mo^{6+} is preserved by increasing the doping content. However, spectral features reflecting the local site symmetry of Mo are different for standards and samples. It is well known that pre-edge feature (20004.9 eV) is associated to 1 s-4d excitation of core electrons to a high-level vacant orbital and, this transition, is only allowed in a tetrahedral field [45,48]. However, it can also be observed in compounds such as MoO_3 because Mo is sited in a distorted octahedral field, allowing thereby admixing of the 4d levels with p orbitals. The intensity of the pre-edge features observed in all LCO-doped samples is reduced compared to that of MoO_3 suggesting a higher site symmetry. In light of these observations, an octahedral coordination environment is preserved in all samples. It is interesting to note that, the LCM005 sample has a higher octahedral distortion compared to LCM010. The enhancement of the catalytic properties in LCM005 occurs in the region of the composition phase diagram where the crystal structure changes from rhombohedral (LCO) to cubic (LCM010), and this region is known as the morphotropic phase boundary. As it has been pointed out before, the catalytic response in this region may be boosted. Due to tetrahedral coordination of Mo in La_2MoO_6, LCMO020 composite has the higher pre-edge intensity than other samples. Moreover, all the samples have similar absorption edge that MoO_3, suggesting that all the Mo existed as Mo^{6+}. The Mo 3d XPS spectra (Fig. S6b) also pointed to same results, that is, all the samples held the single binding energy peak at 232.3 eV and, therefore, the same oxidation state. The Co 2p XPS spectra was also shown in Fig. S6a, where the binding energy peak located at 779.7 eV, 789.4 eV, 794.8 eV and 805.0 eV can be assigned to $2p_{3/2}$, $2p_{3/2}$ satellite (sat.), $2p_{1/2}$ and $2p_{1/2}$ sat. The $3d_{5/2}$ of La 3d XPS spectra (Fig. S6d) can be deconvoluted to 4 components, which indicate the lattice La, surface La species and corresponding satellite.

The EXAFS analysis was also performed after data normalization and background removal. The Fourier Transform (FT) of the $k^3\chi(k)$ spectra were performed in the k-range 3–13.5 $Å^{-1}$ and the plots are shown in Fig. 6c and 6d. For the Co K-edge, the peaks at 1.5, 3.1, 3.5 Å can be assigned to Co-O, Co-La and Co-Co shells. For the Mo K-edge, the peaks at 1.3 and 3.1 Å can be assigned to Mo-O and Mo-La shells. The fitting was further conducted and the detailed procedure is provided in the Text S2. The most intense single scattering paths of the crystalline phase were used to fit the data and the fitting results were in well agreement with previous XRD refinement results. In all samples Co ions are found in octahedral coordination with O ions, as expected from the crystallographic data and in agreement with the low intensity of the pre-edge peak of XANES spectra. As shown in Fig. S7 and Table S5, the Co-O bond distance is 1.927 Å for the LCO sample and it increases gradually with Mo-doping up to reach the value of 1.944 Å for LCMO020. This is a further indication of the Co reduction as observed from the analysis of XANES spectra. The Co-La and Co-Co bond distance also increases gradually with Mo content.

We have also checked the spin state of Co by comparing the magnetic moment of LCO, LCMO005 and LCMO010 (Fig. S8). The detailed procedure to calculate the experimental effective magnetic moment and possible theoretical magnetic moment of Co is provided in Text S3 and the results are shown in Table S6. Considering the increasing ratio of Co^{2+} with the increase of Mo doping as well as the fact that Co^{2+} will always stabilize in high spin state (HS, with a theoretical magnetic moment of 3.87 μ_B), Co^{3+} was found to slightly transfer from HS to low spin state (LS).

To study the cations variation during PMS activation, thus identify the real active sites, XAS measurements at Co K-edge and Mo K-edge were conducted with LCMO005 after the catalytic degradation experiment. As shown in Fig. S10a, an obvious shift to higher energy in absorption edge is observed after the catalytic reaction, suggesting the oxidation of Co. The XANES at Mo K-edge (shown in Fig. S10b) retains similar features after the reaction, except a slightly more intense pre-edge, which can be attributed to the increasing distorted Mo octahedron. The FT modulus of the $k^3\chi(k)$ spectra at Co K-edge and Mo K-edge are also shown in Fig. S10c and d, indicating that no obvious structural change happened after reaction, agreeing with the XRD results (shown in Fig. 8a).

Based on the above analysis, it can be concluded that PMS activation by $LaCo_{1-x}Mo_xO_{3-\delta}$ ($x = 0, 0.05, 0.1$ and 0.2) perovskites takes place through a radical process (Scheme 1). PMS can be better activated by the lower Co oxidation state on the catalyst surface to form reactive radicals like $SO_4\bullet^-$ and •OH via Eq. (1). In the meantime, Co^{3+} were subsequently reduced by HSO_5^- (Eq. (2)) and •OH could oxidize SO_4^{2-} to generate $SO_4\bullet^-$ (Eq. (3)). Due to the fact that Mo remained unchanged before and after reaction, the Co located in B-site was considered as more active site for PMS activation and the role of Mo^{6+}/Mo^{5+} redox cycle seems to be negligible (Eq. (4)). Besides, $^1O_2$ can be formed by the self-decomposition of PMS (Eq. (5) and (6)) contributing to the oxidation of the target pollutant. As it has already been presented in Fig. 3a, increasing Mo dopant to 10% cannot further enhance paracetamol removal. Although the ratio of Co^{2+} is higher than that of LCM005 compound, the higher “oxygen surface” component observed in LCM005 increased the number of active sites for PMS activation [49,50]. It has been reported that these defects could trap PMS on the surface of catalysts [51], thus facilitating the transfer of electron donated from Co cations (Eq. (7) and (8)) [52]. The presence of these local inhomogeneities is usually common in the MPB region.

$$\equiv Co^{2+}/Mo^{5+} + HSO_5^- \rightarrow \equiv Co^{3+}/Mo^{6+} + SO_4^{\cdot-}\left(SO_4^{2-}\right) + OH^-\ (\cdot OH) \tag{1}$$

$$\equiv Co^{3+}/Mo^{6+} + HSO_5{}^- \rightarrow \equiv Co^{2+}/Mo^{5+} + SO_5\bullet^- + H^+ \tag{2}$$

$$SO_4^{2-} + \cdot OH \rightarrow SO_4^{\cdot-} + OH^- \tag{3}$$

$$\equiv Mo^{5+} + \equiv Co^{3+} \rightarrow \equiv Mo^{6+} + \equiv Co^{2+} \tag{4}$$

$$HSO_5{}^- \rightarrow SO_5{}^{2-} + H^+ \tag{5}$$

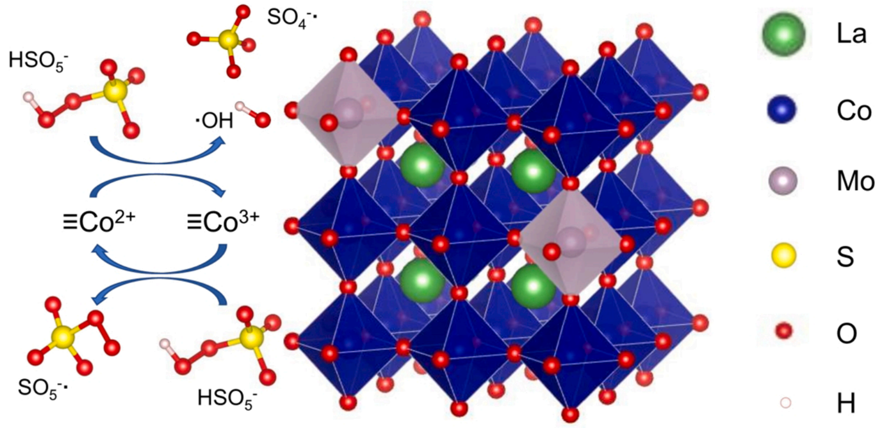

Scheme 1. Proposed PMS activation mechanism via LCMO005.

$$SO_5^{2-} + HSO_5^- \rightarrow HSO_4^- + SO_4^{2-} + {}^1O_2 \quad (6)$$

$$\equiv Co^{2+}/Mo^{6+} + HSO_5^- + V_o \rightarrow \equiv Co^{3+} + SO_4^- + H^+ + O^{2-} \quad (7)$$

$$SO_5^- + O^{2-} \rightarrow SO_4^- + O_2 + V_o \quad (8)$$

3.4. *Catalytic degradation of paracetamol in different operation conditions*

LCMO005 was selected to conduct the degradation experiments under different operation conditions with suspended catalyst. As shown in Fig. 7, the paracetamol removal efficiency could be affected by catalyst and PMS dosages, initial pH and co-existing ions. Fig. 7a illustrates the effect of the catalyst dosage. The paracetamol removal improved from 75.1% to 96.3% within 10 min when the catalyst dosage increased from 0.1 to 0.2 g/L (the inset shows the corresponding increase of k_{obs} from 0.12 to 0.28 min^{-1}), which may be attributed to the increase of active sites for PMS activation. Increasing further the catalyst dosage from 0.2 g/L to 0.5 g/L pointed out to a monotonous improvement of the efficiency, with k_{obs} values rising from 0.28 to 0.41 min^{-1}. This may be due to the fact that the catalyst dosage provided sufficient reactive sites and the reaction rate was limited by the PMS concentration rather than by the density of reactive sites.

Fig. 7b presents paracetamol degradation results with different PMS dosage (0.1 mM – 1 mM). It can be observed that the paracetamol degradation efficiency is enhanced with increasing PMS dosage. When PMS dosage reached 0.5 mM, 96% paracetamol removal was achieved in 10 min with a corresponding k_{obs} increase from 0.28 min^{-1} to 0.5 min^{-1} for PMS dosages ranging from 0.5 mM to 1 mM. The catalyst clearly failed in the complete degradation of paracetamol when PMS dosage was equal or under 0.3 mM. Since the activation mechanism is based on ROS generation, such low PMS concentrations cannot be considered as a sufficient source of oxidizing species in darkness.

pH is an important parameter in PMS activation for the removal of organic pollutants due to the different species present in solution [53]. The initial pH of 10 mg/L paracetamol solution with 0.2 g/L of catalyst and 0.5 mM of PMS amounted to 3.3. The solution pH was adjusted to neutral (7 ± 0.2) before all degradation experiments using 1 M of HNO_3 and 1 M of NaOH solutions. Considering the tiny demand of HNO_3 during pH adjustment, the oxidant character of nitrate anions could be neglected [54]. The effect of initial pH on paracetamol removal is depicted in Fig. 7c. The paracetamol removal was highly acceptable for pH values between 3 and 9 while an inhibitory effect was observed when pH reached 11. This could be interpreted as the pH affected the presence of the major species in PMS solution [52,55]. When the pH is in the range 3–9, PMS mainly existed as HSO_5^{2-} ($pK_{a1}(H_2SO_5) < 0$, $pK_{a2}(H_2SO_5) = 9.4$) [56]. When the pH increased to 11, SO_5^{2-} would be the predominant species, which would not favor ROS generation compared with HSO_5^{2-} [57,58]. The zeta potential was measured in dilute suspensions in electrophoretic cuvettes by adding KNO_3 up to a final concentration of 1 mM. Two supernatant aliquots of each perovskite compound were measured. According to the design specifications of the Zeta Plus device, the electrophoretic velocity is the quantitative observable, allowing to estimate the particle mobilities μe. The relation between zeta potential ζ, and μ_e depends however on a theoretical model [37]. For charged colloidal particles in the viscous drag regime, the Smoluchowski limit is considered most often $\mu_e = \epsilon\zeta/\eta$ (being ϵ the dielectric permittivity, and η the viscosity of the suspending solvent; for nanoparticles dispersed in

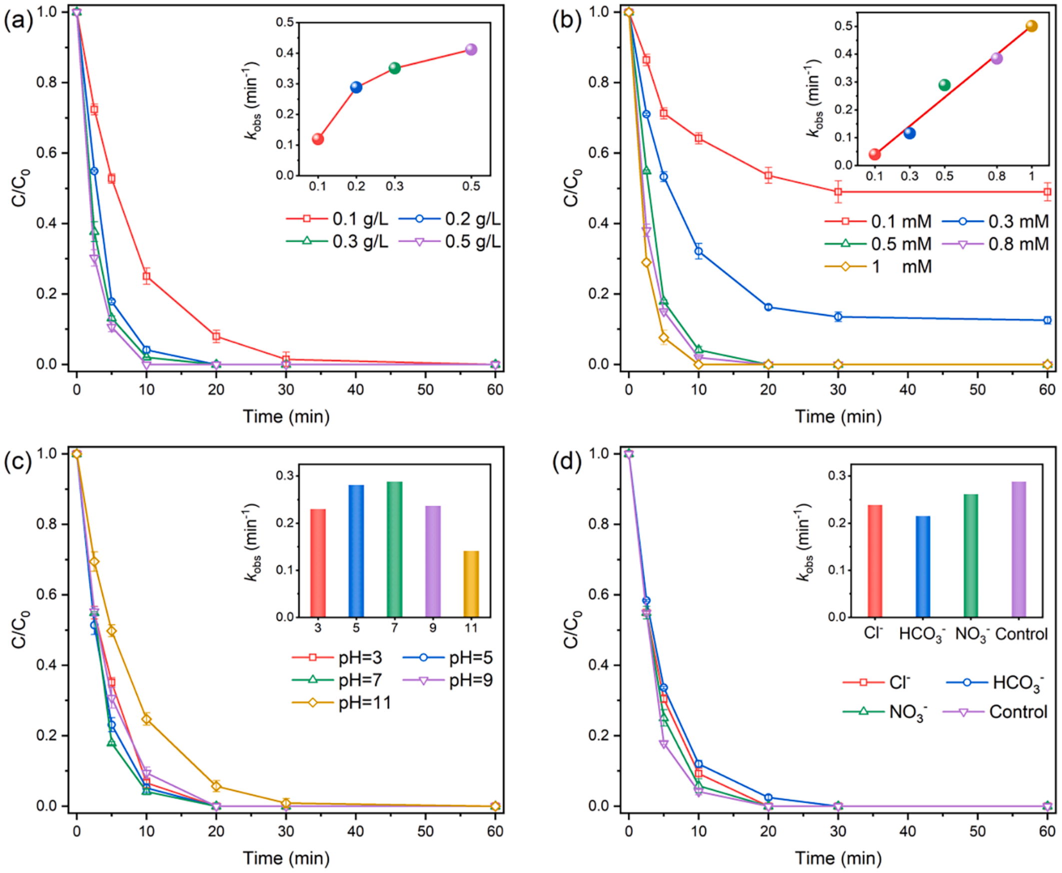

Fig. 7. Effect of catalyst dosage (a), PMS dosage (b), different pH (c) and co-exist anions (2 mM) (d) in paracetamol removal with LCMO005 as catalyst (The inset shows corresponding reaction rate constant). Reaction conditions: [catalyst] = 0.2 g/L (b, c and d), [PMS] = 0.5 mM (a, c and d), [paracetamol] = 10 mg/L, temperature = 25 ± 0.5 °C, initial pH = 7 ± 0.2 (a, b and d).

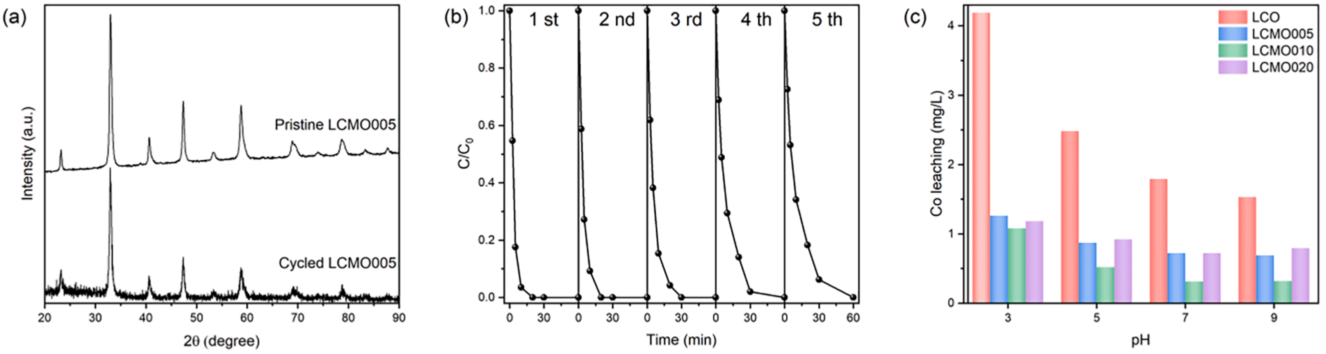

Fig. 8. (a) XRD pattern of pristine and cycled LCMO005. (b) Effect of experiment cycles on paracetamol removal. (c) Co leaching of LCO, LCMO005, LCMO010 and LCMO020 at different initial pH. Reaction conditions: [catalyst] = 0.2 g/L, [PMS] = 0.5 mM, [paracetamol] = 10 mg/L, temperature = 25 ± 0.5 °C, initial pH = 7 ± 0.2 for (a).

aqueous KNO_3 solution $\epsilon = 78{,}5\ \epsilon_0$ and $\eta = 10^{-3}$ Pa s). Table S7 collects the experimental results obtained for the four perovskite synthesis outcomes. Negative zeta potential values have been found for all the perovskites except for the LCMO005 compound that has a neutral charge.

The effect of Cl^-, HCO_3^- and NO_3^- on paracetamol removal was further investigated. As shown in Fig. 7d, the paracetamol removal efficiency is not overmuch affected in the presence of 2 mM Cl^-, HCO_3^- and NO_3^-. Among these coexisting anions, the presence of HCO_3^- and Cl^- may also participate in the direct decomposition of PMS to generate weaker oxidants and radicals ($Cl^\bullet$, $CO_3^{\bullet-}$, etc.) instead of $SO_4^{\bullet-}$ and $^\bullet OH$ [16,33,59]. The HCO_3^- appeared higher scavenging effect while the Cl^- and NO_3^- hardly affect the paracetamol removal when the concentration increased to 10 mM (Fig. S9). To test the effect of natural organic matter (NOM), the paracetamol removal experiments were performed with 10 mM humic acid (HA) as representative NOM. It has been reported that the quinones/semiquinones functional groups in HA may act as PMS activator [60]. As shown in Fig. S9, the paracetamol removal was slightly inhibited with 10 mM HA, which can be attributed to the scavenging effect due to the competitive reaction with $SO_4^{\bullet-}$ and $^\bullet OH$ [12].

3.5. Reusability and stability test

Recycling experiments were conducted to evaluate the reusability of LCMO005 as catalyst. The XRD pattern of cycled LCMO005 (Fig. 8a) demonstrated that there was no obvious structural change after the experiments of consecutive cycles. As shown in Fig. 8b, the paracetamol removal efficiency slightly decreased along with consecutive reaction cycles, reaching ~ 95% paracetamol removal in 30 min for the 5th cycle. We have also tested the Co leaching at different initial pH values to check the solubility of all the samples. Fig. 8c shows that leaching of Co was significantly reduced by doping LCO with Mo. Moreover, 0.196 mg/L Mo leaching was observed with LCMO005 as the catalyst at pH 7. It is worth noting that metal leaching in doped samples is below 1 mg/L even at pH values as low as 5, that is a clear indication of the high stability attained in the doped samples.

3.6. Performance of deposited LCMO005 perovskite in a Lab-grade photoreactor with LED technology

In order to eliminate a later separation stage, necessary to remove the suspended catalyst from the medium after treatment, LCMO005 was deposited on a cylindrical titanium plate, as explained in the methodology section. Fig. 9a shows the results of paracetamol degradation (initial concentration of 10 mg/L) obtained in the photoreactor when PMS (0.5 mM), UVA or UVC radiations are applied. It is observed a negligible degradation of the pollutant through the photocatalytic process, that is, without PMS in the reaction medium. As expected, a fast removal of paracetamol takes places with PMS in darkness due to the rapid generation of ROS by the catalyst as demonstrated by our batch laboratory previous experiments. Interestingly, LCMO005 perovskite presented a slightly higher performance when it is deposited in the reactor rather than in suspension, indicating that the deposition process did not affect PMS activation. The best degradation results were obtained by the combination of PMS with UVC radiation. The degradation

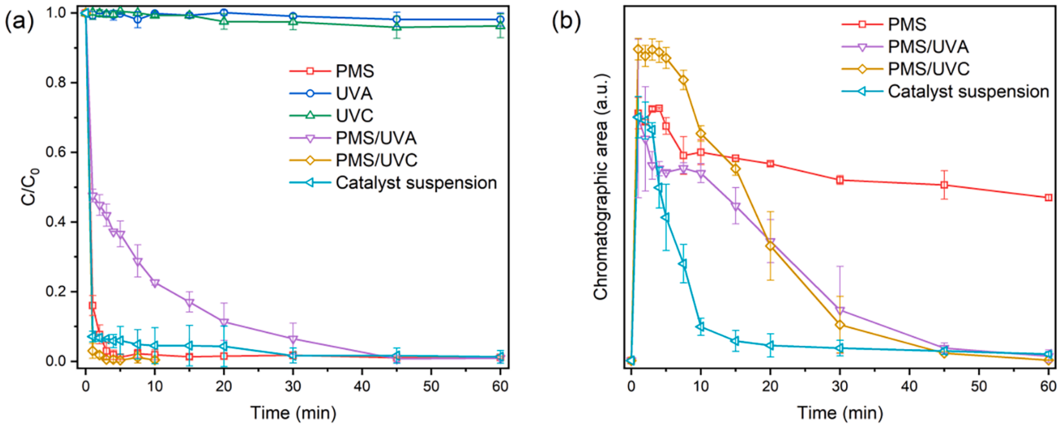

Fig. 9. Paracetamol removal (a) and reaction intermediate profile (b) with deposited LCMO005 and catalyst suspension (The catalyst suspension experiment also includes UVC irradiation). Reaction conditions: [catalyst] = 0.3 g/L, [PMS] = 0.5 mM, [paracetamol] = 10 mg/L, temperature = 25 ± 0.5 °C. UVA: 20 LEDs, 365–370 nm, 1200 mW, 2100 W/m^2. UVC: 20 LEDs, 265–280 nm, 15 mW, 25 W/m^2.

kinetics is so fast that, paracetamol, can hardly be detected in the first minute of the degradation process. Surprisingly, the combination of PMS with UVA entails a slower paracetamol removal compared to the experiments conducted in dark conditions. In order to shed light into this inconsistent behavior, we have followed the chromatographic area of an intermediate compound (retention time: 1.5 min) formed during the degradation process. Fig. 9b shows that the fast degradation of paracetamol with PMS/UVC produces a high concentration of the intermediate product at initial reaction times, followed by a progressive mineralization that is finally reached in 50 min This fact demonstrates the synergetic effect that exists between UVC radiation and PMS activation on the catalyst surface that enhances, not only the decomposition of paracetamol, but also the abatement of the different generated organic compounds, such as reaction intermediates [61–63]. The test conducted with PMS and UVA shows a more complicated degradation process that affects paracetamol and intermediates in a different manner. Firstly, paracetamol degradation is dominant at the early stage of PMS/UVA process but, as soon as the intermediate is generated, ROS species may be involved in an oxidation competition for the degradation of the target pollutant and the intermediate product. It is worth mentioning that such competition was not observed in the PMS/UVC degradation profile because of its high energy radiation. Paracetamol degradation is observed at 30 min and, complete mineralization of the intermediate is also reached in 50 min. On the other hand, although paracetamol degradation can be easily attained in the photoreactor with PMS in darkness, the intermediate cannot be completely removed from the solution due to the strong recalcitrant character of this byproduct. A more efficient removal of the formed reaction intermediate is found when the catalyst is used in suspension (Fig. 9b), although a turbidity of 72.02 FTU was observed, which could reduce the action of UV radiation. It is also important to take into account that the process efficiency can be decreased when the catalyst is deposited, because of the important contribution of the mass transfer control to the process kinetics.

4. Conclusions

In this work, $LaCo_{1-x}Mo_xO_{3-\delta}$ perovskites were demonstrated to be efficient catalysts for PMS activation in darkness. >98% paracetamol can be removed in 10 min with $LaCo_{0.95}Mo_{0.05}O_{3-\delta}$ (LCMO005) at optimum conditions (0.2 g/L of catalyst, 0.5 mM (0.153 g/L) of PMS and 10 mg/L of paracetamol), increasing 2.6 times the kinetic degradation constant from that of the undoped $LaCoO_{3-\delta}$ perovskite. The reduction of cobalt oxidation state in LCMO005, promoted by molybdenum doping, is the responsible of the PMS activation. A dominant sulfate radical pathway was clearly identified in all the $LaCo_{1-x}Mo_xO_{3-\delta}$/PMS system. Furthermore, the higher performance of LCMO005 catalysts can be understood in terms of the vicinity of a compositional morphotropic phase boundary between rhombohedral and cubic phases. We have also tested the performance of deposited LCMO005 perovskite in a Lab-grade photoreactor with LED technology obtaining superior results in the complete removal of paracetamol and corresponding intermediates with PMS/UVC in scarcely 30 min. In summary, our work highlights the crucial role of high valence state TMs doping and provide new insight into rational PMS activator design.

Declaration of Competing Interest

The authors declare that they have no known competing financial interests or personal relationships that could have appeared to influence the work reported in this paper.

Acknowledgments

Yu Shen acknowledges support from the China Scholarship Council (CSC) scholarship (201807040073). Authors are also indebted with Spanish Ministerio de Ciencia e Innovación (MICINN) for funding through the grant number MAT2017-84385-R and Fundación Ramón Areces through PR2007-18/02 project. XAS experiments were performed at the CLÆSS beamline at ALBA Synchrotron with the collaboration of ALBA staff. Studies with deposited catalyst were conducted at the Universidad de Cantabria (Spain) from the “Supports for short stays of researchers from other institutions at the Universidad de Cantabria during the year 2021”. We want also to acknowledge support from Prof. E. Enciso Rodríguez (UCM) in the determination of Zeta potential of the perovskites.

Appendix A. Supplementary data

Supplementary data to this article can be found online at https://doi.org/10.1016/j.cej.2022.137352.

References

[1] N.H. Tran, M. Reinhard, K.-Y.-H. Gin, Occurrence and fate of emerging contaminants in municipal wastewater treatment plants from different geographical regions-a review, Water Res. 133 (2018) 182–207.
[2] L. Yang, L.E. Yu, M.B. Ray, Degradation of paracetamol in aqueous solutions by TiO2 photocatalysis, Water Res. 42 (13) (2008) 3480–3488.
[3] M.A. Oturan, J.-J. Aaron, Advanced oxidation processes in water/wastewater treatment: principles and applications A Review, Critical Reviews in Environmental Science and Technology 44 (2014) 2577–2641.
[4] F. Guo, X. Huang, Z. Chen, L. Cao, X. Cheng, L. Chen, W. Shi, Construction of Cu3P-ZnSnO3-g-C3N4 p-n-n heterojunction with multiple built-in electric fields for effectively boosting visible-light photocatalytic degradation of broad-spectrum antibiotics, Sep. Purif. Technol. 265 (2021), 118477.
[5] N. Cao, M. Gu, M. Gao, C. Li, K. Liu, X. Zhao, J. Feng, Y. Ren, T. Wei, A three-layer photocatalyst carbon fibers/TiO2 seed/TiO2 nanorods with high photocatalytic degradation under visible light, Appl. Surf. Sci. 530 (2020), 147289.
[6] J. Pan, F. Guo, H. Sun, Y. Shi, W. Shi, Nanodiamonds anchored on porous ZnSnO3 cubes as an efficient composite photocatalyst with improved visible-light photocatalytic degradation of tetracycline, Sep. Purif. Technol. 263 (2021), 118398.
[7] J. Wang, S. Wang, Reactive species in advanced oxidation processes: Formation, identification and reaction mechanism, Chem. Eng. J. 401 (2020), 126158.
[8] Q. Yang, H. Choi, S.R. Al-Abed, D.D. Dionysiou, Iron–cobalt mixed oxide nanocatalysts: Heterogeneous peroxymonosulfate activation, cobalt leaching, and ferromagnetic properties for environmental applications, Appl. Catal. B 88 (2009) 462–469.
[9] Y. Shen, M.J. Martín de Vidales, J.C. Espíndola, A. Gómez-Herrero, A.j., Dos santos-García, Paracetamol degradation by photo-assisted activation of peroxymonosulfate over ZnxNi1−xFe2O4@BiOBr heterojunctions, J. Environ. Chem. Eng. 9 (2021), 106797.
[10] R. Xiao, Z. Luo, Z. Wei, S. Luo, R. Spinney, W. Yang, D.D. Dionysiou, Activation of peroxymonosulfate/persulfate by nanomaterials for sulfate radical-based advanced oxidation technologies, Curr. Opin. Chem. Eng. 19 (2018) 51–58.
[11] W.-D. Oh, Z. Dong, T.-T. Lim, Generation of sulfate radical through heterogeneous catalysis for organic contaminants removal: Current development, challenges and prospects, Appl. Catal. B 194 (2016) 169–201.
[12] S. Wacławek, H.V. Lutze, K. Grübel, V.V.T. Padil, M. Černík, D.D. Dionysiou, Chemistry of persulfates in water and wastewater treatment: A review, Chem. Eng. J. 330 (2017) 44–62.
[13] J. Lee, U. von Gunten, J.-H. Kim, Persulfate-Based Advanced Oxidation: Critical Assessment of Opportunities and Roadblocks, Environ. Sci. Technol. 54 (2020) 3064–3081.
[14] F. Ghanbari, M. Moradi, Application of peroxymonosulfate and its activation methods for degradation of environmental organic pollutants: Review, Chem. Eng. J. 310 (2017) 41–62.
[15] Y. Zhao, H. An, G. Dong, J. Feng, T. Wei, Y. Ren, J. Ma, Oxygen vacancies induced heterogeneous catalysis of peroxymonosulfate by Ni-doped AgFeO2 materials: Evolution of reactive oxygen species and mechanism, Chem. Eng. J. 388 (2020), 124371.
[16] P. Hu, M. Long, Cobalt-catalyzed sulfate radical-based advanced oxidation: A review on heterogeneous catalysts and applications, Appl. Catal. B 181 (2016) 103–117.
[17] K. Wang, C. Han, Z. Shao, J. Qiu, S. Wang, S. Liu, Perovskite Oxide Catalysts for Advanced Oxidation Reactions, Adv. Funct. Mater. 31 (2021) 2102089.
[18] X. Duan, C. Su, J. Miao, Y. Zhong, Z. Shao, S. Wang, H. Sun, Insights into perovskite-catalyzed peroxymonosulfate activation: Maneuverable cobalt sites for promoted evolution of sulfate radicals, Appl. Catal. B 220 (2018) 626–634.
[19] R. Mitchell, Perovskites: Modern and Ancient Almaz Press Inc, Ontario, Canada, 2002.
[20] E. Solana-Madruga, Á.M. Arévalo-López, A.J. DosSantos-García, E. Urones-Garrote, D. Ávila-Brande, R. Sáez-Puche, J.P. Attfield, Double Double Cation Order in the High-Pressure Perovskites MnRMnSbO6, Angew. Chem. Int. Ed. 55 (32) (2016) 9340–9344.
[21] J. Ricote, D.L. Corker, R.W. Whatmore, S.A. Impey, A.M. Glazer, J. Dec, K. Roleder, A TEM and neutron diffraction study of the local structure in the rhombohedral

phase of lead zirconate titanate, J. Phys.: Condens. Matter 10 (8) (1998) 1767–1786.

[22] T.-F. Zhang, X.-G. Tang, Q.-X. Liu, S.-G. Lu, Y.-P. Jiang, X.-X. Huang, Q.-F. Zhou, Oxygen-vacancy-related relaxation and conduction behavior in (Pb1-xBax)(Zr0.95Ti0.05)O3 ceramics, AIP Adv. 4 (2014), 107141.

[23] X. Pang, Y. Guo, Y. Zhang, B. Xu, F. Qi, LaCoO3 perovskite oxide activation of peroxymonosulfate for aqueous 2-phenyl-5-sulfobenzimidazole degradation: Effect of synthetic method and the reaction mechanism, Chem. Eng. J. 304 (2016) 897–907.

[24] T. Chen, J. Miao, M. Zhu, R. Ran, W. Zhou, Z. Shao, Thermal reduction-assisted electronic structure tuning of perovskite oxide as catalyst for efficient advanced oxidation, Compos. B Eng. 207 (2021), 108577.

[25] P. Liang, D. Meng, Y. Liang, Z. Wang, C. Zhang, S. Wang, Z. Zhang, Cation deficiency tuned LaCoO3−δ perovskite for peroxymonosulfate activation towards bisphenol A degradation, Chem. Eng. J. 409 (2021), 128196.

[26] C. Gkika, A. Petala, Z. Frontistis, G. Bampos, D. Hela, I. Konstantinou, D. Mantzavinos, Heterogeneous activation of persulfate by lanthanum strontium cobaltite for sulfamethoxazole degradation, Catal. Today 361 (2021) 130–138.

[27] J. Miao, J. Sunarso, C. Su, W. Zhou, S. Wang, Z. Shao, SrCo1−xTixO3−δ perovskites as excellent catalysts for fast degradation of water contaminants in neutral and alkaline solutions, Sci. Rep. 7 (2017) 44215.

[28] M. Zhu, D. Guan, Z. Hu, H.-J. Lin, C.-T. Chen, H.-S. Sheu, S. Wang, J. Zhou, W. Zhou, Z. Shao, Synergistic effects in ordered Co oxides for boosting catalytic activity in advanced oxidation processes, Appl. Catal. B 297 (2021), 120463.

[29] Y. Wang, Z. Chi, C. Chen, C. Su, D. Liu, Y. Liu, X. Duan, S. Wang, Facet- and defect-dependent activity of perovskites in catalytic evolution of sulfate radicals, Appl. Catal. B 272 (2020), 118972.

[30] C. Su, X. Duan, J. Miao, Y. Zhong, W. Zhou, S. Wang, Z. Shao, Mixed Conducting Perovskite Materials as Superior Catalysts for Fast Aqueous-Phase Advanced Oxidation: A Mechanistic Study, ACS Catal. 7 (1) (2017) 388–397.

[31] S. Lu, G. Wang, S. Chen, H. Yu, F. Ye, X. Quan, Heterogeneous activation of peroxymonosulfate by LaCo1-xCuxO3 perovskites for degradation of organic pollutants, J. Hazard. Mater. 353 (2018) 401–409.

[32] R.D. Shannon, Revised effective ionic radii and systematic studies of interatomic distances in halides and chalcogenides, Acta Crystallographica Section A 32 (5) (1976) 751–767.

[33] Z.-Y. Guo, C.-X. Li, M. Gao, X. Han, Y.-J. Zhang, W.-J. Zhang, W.-W. Li, Mn−O Covalency Governs the Intrinsic Activity of Co-Mn Spinel Oxides for Boosted Peroxymonosulfate Activation, Angew. Chem. Int. Ed. 60 (1) (2021) 274–280.

[34] J. Rodríguez-Carvajal, Recent advances in magnetic structure determination by neutron powder diffraction, Physica B 192 (1993) 55–69.

[35] B. Ravel, M. Newville, ATHENA, ARTEMIS, HEPHAESTUS: data analysis for X-ray absorption spectroscopy using IFEFFIT, Journal of Synchrotron Radiation 12 (2005) 537–541.

[36] C. Liang, C.-F. Huang, N. Mohanty, R.M. Kurakalva, A rapid spectrophotometric determination of persulfate anion in ISCO, Chemosphere 73 (9) (2008) 1540–1543.

[37] R.J. Hunter, Zeta potential in colloid science: principles and applications, Academic press2013.

[38] X. Li, S. Wang, H. An, G. Dong, J. Feng, T. Wei, Y. Ren, J. Ma, Enhanced photocatalytic reduction of nitrate enabled by Fe-doped LiNbO3 materials in water: Performance and mechanism, Appl. Surf. Sci. 539 (2021) 148257.

[39] P. Gao, X. Tian, W. Fu, Y. Wang, Y. Nie, C. Yang, Y. Deng, Copper in LaMnO3 to promote peroxymonosulfate activation by regulating the reactive oxygen species in sulfamethoxazole degradation, J. Hazard. Mater. 411 (2021), 125163.

[40] Q. Pan, Q. Gao, G. Gao, M. Liu, B. Han, K. Xia, C. Zhou, Composition-engineered LaCoO3-based monolithic catalysts for easily operational and robust peroxymonosulfate activation, Chem. Eng. J. 424 (2021), 130574.

[41] Y.i. Yang, G. Banerjee, G.W. Brudvig, J.-H. Kim, J.J. Pignatello, Oxidation of Organic Compounds in Water by Unactivated Peroxymonosulfate, Environ. Sci. Technol. 52 (10) (2018) 5911–5919.

[42] C. Li, Y. Huang, X. Dong, Z. Sun, X. Duan, B. Ren, S. Zheng, D.D. Dionysiou, Highly efficient activation of peroxymonosulfate by natural negatively-charged kaolinite with abundant hydroxyl groups for the degradation of atrazine, Appl. Catal. B 247 (2019) 10–23.

[43] W. Tan, W. Ren, C. Wang, Y. Fan, B. Deng, H. Lin, H. Zhang, Peroxymonosulfate activated with waste battery-based Mn-Fe oxides for pollutant removal: Electron transfer mechanism, selective oxidation and LFER analysis, Chem. Eng. J. 394 (2020), 124864.

[44] Y.-Y. Ahn, H. Bae, H.-I. Kim, S.-H. Kim, J.-H. Kim, S.-G. Lee, J. Lee, Surface-loaded metal nanoparticles for peroxymonosulfate activation: Efficiency and mechanism reconnaissance, Appl. Catal. B 241 (2019) 561–569.

[45] T. Yamamoto, Assignment of pre-edge peaks in K-edge x-ray absorption spectra of 3d transition metal compounds: electric dipole or quadrupole? X-Ray Spectrom. 37 (6) (2008) 572–584.

[46] H. Liang, Y. Hong, C. Zhu, S. Li, Y. Chen, Z. Liu, D. Ye, Influence of partial Mn-substitution on surface oxygen species of LaCoO3 catalysts, Catal. Today 201 (2013) 98–102.

[47] K.A. Stoerzinger, W.T. Hong, E.J. Crumlin, H. Bluhm, M.D. Biegalski, Y. Shao-Horn, Water Reactivity on the LaCoO3 (001) Surface: An Ambient Pressure X-ray Photoelectron Spectroscopy Study, The Journal of Physical Chemistry C 118 (2014) 19733–19741.

[48] J.A. Wharton, D.H. Ross, G.M. Treacy, G.D. Wilcox, K.R. Baldwin, An EXAFS investigation of molybdate-based conversion coatings, J. Appl. Electrochem. 33 (2003) 553–561.

[49] P. Li, Y. Lin, S. Zhao, Y. Fu, W. Li, R. Chen, S. Tian, Defect-engineered Co3O4 with porous multishelled hollow architecture enables boosted advanced oxidation processes, Appl. Catal. B 298 (2021), 120596.

[50] H. Zhang, C. Li, L. Lyu, C. Hu, Surface oxygen vacancy inducing peroxymonosulfate activation through electron donation of pollutants over cobalt-zinc ferrite for water purification, Appl. Catal. B 270 (2020), 118874.

[51] N. Cao, X. Zhao, M. Gao, Z. Li, X. Ding, C. Li, K. Liu, X. Du, W. Li, J. Feng, Y. Ren, T. Wei, Superior selective adsorption of MgO with abundant oxygen vacancies to removal and recycle reactive dyes, Sep. Purif. Technol. 275 (2021), 119236.

[52] Y. Ren, L. Lin, J. Ma, J. Yang, J. Feng, Z. Fan, Sulfate radicals induced from peroxymonosulfate by magnetic ferrospinel MFe2O4 (M=Co, Cu, Mn, and Zn) as heterogeneous catalysts in the water, Appl. Catal. B 165 (2015) 572–578.

[53] G.P. Anipsitakis, D.D. Dionysiou, Degradation of Organic Contaminants in Water with Sulfate Radicals Generated by the Conjunction of Peroxymonosulfate with Cobalt, Environ. Sci. Technol. 37 (20) (2003) 4790–4797.

[54] Y. Yao, H. Chen, J. Qin, G. Wu, C. Lian, J. Zhang, S. Wang, Iron encapsulated in boron and nitrogen codoped carbon nanotubes as synergistic catalysts for Fenton-like reaction, Water Res. 101 (2016) 281–291.

[55] K.H. Chan, W. Chu, Degradation of atrazine by cobalt-mediated activation of peroxymonosulfate: Different cobalt counteranions in homogenous process and cobalt oxide catalysts in photolytic heterogeneous process, Water Res. 43 (2009) 2513–2521.

[56] E.A. Betterton, M.R. Hoffmann, Oxidation of aqueous sulfur dioxide by peroxymonosulfate, The Journal of Physical Chemistry 92 (21) (1988) 5962–5965.

[57] Y.-H. Guan, J. Ma, Y.-M. Ren, Y.-L. Liu, J.-Y. Xiao, L.-Q. Lin, C. Zhang, Efficient degradation of atrazine by magnetic porous copper ferrite catalyzed peroxymonosulfate oxidation via the formation of hydroxyl and sulfate radicals, Water Res. 47 (14) (2013) 5431–5438.

[58] A. Rastogi, S.R. Al-Abed, D.D. Dionysiou, Sulfate radical-based ferrous–peroxymonosulfate oxidative system for PCBs degradation in aqueous and sediment systems, Appl. Catal. B 85 (2009) 171–179.

[59] G.P. Anipsitakis, D.D. Dionysiou, M.A. Gonzalez, Cobalt-Mediated Activation of Peroxymonosulfate and Sulfate Radical Attack on Phenolic Compounds, Implications of Chloride Ions, Environmental Science & Technology 40 (3) (2006) 1000–1007.

[60] G. Fang, J. Gao, D.D. Dionysiou, C. Liu, D. Zhou, Activation of Persulfate by Quinones: Free Radical Reactions and Implication for the Degradation of PCBs, Environ. Sci. Technol. 47 (2013) 4605–4611.

[61] C. Tan, X. Jian, L. Su, X. Lu, J. Huang, J. Deng, W. Chu, Kinetic removal of acetaminophen and phenacetin during LED-UV365 photolysis of persulfate system: Reactive oxygen species generation, Chemosphere 269 (2021), 129337.

[62] G. Moussavi, H. Momeninejad, S. Shekoohiyan, P. Baratpour, Oxidation of acetaminophen in the contaminated water using UVC/S2O82− process in a cylindrical photoreactor: Efficiency and kinetics of degradation and mineralization, Sep. Purif. Technol. 181 (2017) 132–138.

[63] M.J.M. de Vidales, C. Sáez, J.F. Pérez, S. Cotillas, J. Llanos, P. Cañizares, M. A. Rodrigo, Irradiation-assisted electrochemical processes for the removal of persistent organic pollutants from wastewater, J. Appl. Electrochem. 45 (7) (2015) 799–808.